The Astrophysical Journal, 626:58–69, 2005 June 10

SPITZER OBSERVATIONS OF OPTICALLY "INVISIBLE" RADIO AND X-RAY SOURCES: HIGH-REDSHIFT ACTIVE GALACTIC NUCLEI

J. L. Higdon,[1] S. J. U. Higdon,[1] D. W. Weedman,[1] J. R. Houck,[1] E. Le Floc'h,[2] M. J. I. Brown,[3] A. Dey,[4] B. T. Jannuzi,[4] B. T. Soifer,[5] and M. J. Rieke[2]

Received 2004 July 25; accepted 2005 January 30

ABSTRACT

We have combined a survey at 24 μm to 0.3 mJy with the Multiband Imaging Photometer (MIPS) on the *Spitzer Space Telescope*, a 20 cm A-configuration Very Large Array (VLA) survey covering 0.5 deg^2, and an existing 172 ks *Chandra X-Ray Observatory* exposure to investigate the nature of optically faint radio and X-ray sources in the NOAO Deep Wide-Field Survey (NDWFS) in the Bootes field. A catalog of 392 radio sources is defined with optical identifications or magnitude limits. We find little overlap between the radio- and infrared-selected populations: only 9% of the infrared sources are detected in the radio, and only 33% of the radio sources are detected in the infrared. Thirty-six (10%) of the 377 compact radio sources lack optical counterparts in the NDWFS B_W, R, and I images. We refer to these objects as optically invisible radio sources (OIRSs). Only four (13%) of the 31 OIRSs observed with MIPS are detected at 24 μm. Comparisons of the radio and infrared properties of the OIRSs with various galaxy spectral energy distributions demonstrate that most of these sources are powered by active galactic nuclei (AGNs) rather than starbursts. Similarly, 11 X-ray sources observed by both MIPS and the VLA are classified as optically invisible X-ray sources (OIXSs). None is detected at 24 μm or 20 cm. All seven OIXSs detected in *Chandra*'s 0.5–2 keV band have infrared to X-ray flux ratios consistent with their luminosity being dominated by an unobscured AGN. From these results we conclude that both the optically invisible radio and X-ray source populations are primarily AGNs, relatively unaffected by dust, and most likely at $z > 1$. No OIRSs are detected in X-ray emission, and no OIXSs are detected at 20 cm. However, given the wide range in radio and X-ray properties of known AGNs and the size of our samples, this lack of overlap does not necessarily imply different AGN source populations.

Subject headings: galaxies: high-redshift — galaxies: starburst — infrared: galaxies — radio continuum: galaxies — X-rays: galaxies

1. INTRODUCTION

Determining the star formation density of the universe beyond $z \sim 1$ and the contribution made by active galactic nuclei (AGNs) to the luminosity evolution of galaxies are two fundamental goals of observational cosmology. Addressing these questions requires observations at wavelengths capable of locating intrinsically luminous sources that are either heavily obscured by dust or so distant that their rest-frame optical wavebands fall below the cutoff for intergalactic hydrogen absorption (i.e., the Lyman limit). Locating and understanding such obscured sources is a fundamental objective of the *Spitzer Space Telescope* (Werner et al. 2004) mission,[6] which is capable of identifying $z > 1$ galaxy populations that are luminous at infrared wavelengths but faint optically because of the effects of dust. Starbursts and AGNs are expected to be powerful emitters at radio wavelengths because of large populations of radio-luminous supernova remnants for starbursts and accretion disk phenomena for AGNs. Indeed, sensitive radio surveys routinely find populations of submillijansky point sources with either very faint optical counterparts or no counterparts at all (e.g., Richards et al. 1999; Fomalont et al. 2002). Whether these sources represent dust-enshrouded starburst galaxies at $z \sim 1-3$ or radio-loud AGNs at $z > 4$ has yet to be determined conclusively. This suggests as a strategy for locating heavily obscured starbursts and AGNs at high redshifts the definition of infrared and radio source populations that are either extremely faint at all optical bands or "invisible," i.e., objects that cannot be distinguished from the background in deep optical images.

The NOAO Deep Wide-Field Survey (NDWFS; Jannuzi & Dey 1999)[7] provides multiband optical imagery to very faint magnitudes over large survey areas and so is uniquely suited for comparison to other surveys in search of sources that are optically invisible. In particular, the NDWFS field in Bootes covers $\sim$9.3 deg^2 to sensitivities in B_W, R, and I of approximately 26.5, 25.5, and 24.7 (Vega) mag, respectively.[8] To explore the mid-infrared characteristics of this data set, we have surveyed most of the Bootes field at wavelengths of 24, 70, and 160 μm with *Spitzer*'s Multiband Imaging Photometer (MIPS; Rieke et al.

[1] Astronomy Department, 610 Space Sciences Building, Cornell University, Ithaca, NY 14853.
[2] Steward Observatory, University of Arizona, 933 North Cherry Avenue, Tucson, AZ 85721.
[3] Department of Astrophysical Sciences, Peyton Hall, Princeton University, Princeton, NJ 08544.
[4] National Optical Astronomy Observatory, 950 North Cherry Avenue, Tucson, AZ 85726.
[5] *Spitzer* Science Center, MC 220-6, California Institute of Technology, 1200 East California Boulevard, Pasadena, CA 91125.
[6] The *Spitzer Space Telescope* is operated by the Jet Propulsion Laboratory, California Institute of Technology, for the National Aeronautics and Space Administration. Information on *Spitzer* can be found at http://ssc.spitzer.caltech.edu/.
[7] The NDWFS is supported by the National Optical Astronomy Observatory, which is operated by the Association of Universities for Research in Astronomy (AURA), Inc., under a cooperative agreement with the National Science Foundation. Information on the NDWFS can be found at http://www.noao.edu/noao/noaodeep/.
[8] These represent the 50% completeness limits in the source catalogs for the area involved in this study. Similar sensitivities are expected throughout the survey.

2004). At 24 μm the point source sensitivity is 0.3 mJy (5 σ), and the angular resolution is 5.″5 (FWHM). We will present other results of this infrared survey in more detail in future publications, although the survey and analysis techniques have been described by Papovich et al. (2004).

Deep and high-resolution radio data are important for a full understanding of the nature of the sources detected by MIPS. This follows from the well-established tight correlation between infrared and radio flux densities in star-forming galaxies (de Jong et al. 1985; Helou et al. 1985), which is a consequence of the life (reradiation of UV photons by dust) and death (SNe remnants) of massive stars. As a result, the ratio of infrared to radio flux densities provides a means of distinguishing starbursts from AGNs. Moreover, the subarcsecond positional accuracy attainable with radio interferometric surveys allows confident matching of sources discovered in infrared surveys, which can have poorer spatial resolution. This is especially important if a source is indeed optically invisible. For these reasons, we conducted sensitive and high angular resolution observations of a 0.5 deg^2 subregion within the Bootes field with the Very Large Array (VLA) at 20 cm. These observations were designed to detect dusty starburst galaxies with 24 μm flux densities greater than 0.75 mJy based on their expected spectral energy distributions and likely redshift range.[9] Although the MIPS 24 μm survey reaches a fainter limit than this, we chose this infrared limit for matching radio observations because we were primarily interested in selecting sources bright enough to obtain spectra with the Infrared Spectrograph (IRS; Houck et al. 2004) on *Spitzer* (i.e., Higdon et al. 2004; Houck et al. 2005).

Our survey region was chosen to overlap the northern Large Area Lyman Alpha survey field (LALA; Rhoads et al. 2000), which includes an extremely deep (172 ks) *Chandra X-Ray Observatory* integration by Wang et al. (2004), centered at R.A. = $14^{\rm h}25^{\rm m}37\overset{\rm s}{.}79$ and decl. = $+35^\circ36'00\overset{''}{.}2$ and covering 0.1 deg^2. The X-ray point source sensitivities are 1.5×10^{-16} ergs s^{-1} cm^{-2} in the "soft" 0.5–2.0 keV band and 1.0×10^{-15} ergs s^{-1} cm^{-2} in the "hard" 2.0–7.0 keV band (both 5 σ). Only the North and South Chandra Deep Fields (2 and 1 Ms integrations, respectively) are substantially deeper. As a result, there was minimal overlap with the much more extensive 20 cm survey of the Bootes field by de Vries et al. (2002) using the Westerbork Synthesis Radio Telescope (WSRT). In this paper we use the combined X-ray, optical, infrared, and radio catalogs to investigate the nature of optically invisible radio and X-ray sources (OIRSs and OIXSs) in our radio survey area. These are defined to be X-ray and compact radio sources that have no apparent counterparts in the NDWFS B_W, R, and I images. In addition, we wish to see how the properties of these two optically invisible populations compare with one another.

The outline of this paper is as follows. We first discuss the VLA observations and data reduction in § 2. This is followed by a brief discussion of the radio source catalog in § 3 and our criteria for matching sources from the MIPS, *Chandra*, and VLA surveys. We then describe the infrared, radio, and X-ray properties of the optically invisible radio and X-ray sources (§ 4) to constrain the dominant source of their luminosity. Finally, before summarizing in § 6, we compare the average space densities of the OIRSs and OIXSs with those of other galaxies, including quasars, and also consider whether OIRSs and OIXSs are drawn from the same population in § 5. Throughout this paper, we have assumed a flat ΛCDM cosmology with $\Omega_M = 0.27$, $\Omega_\Lambda = 0.73$, and a Hubble constant of 71 km s^{-1} Mpc^{-1}.

[9] For these estimates we used the starburst infrared/radio correlation of Yun et al. (2001) together with *K*-corrections from the SED templates of Lagache et al. (2003).

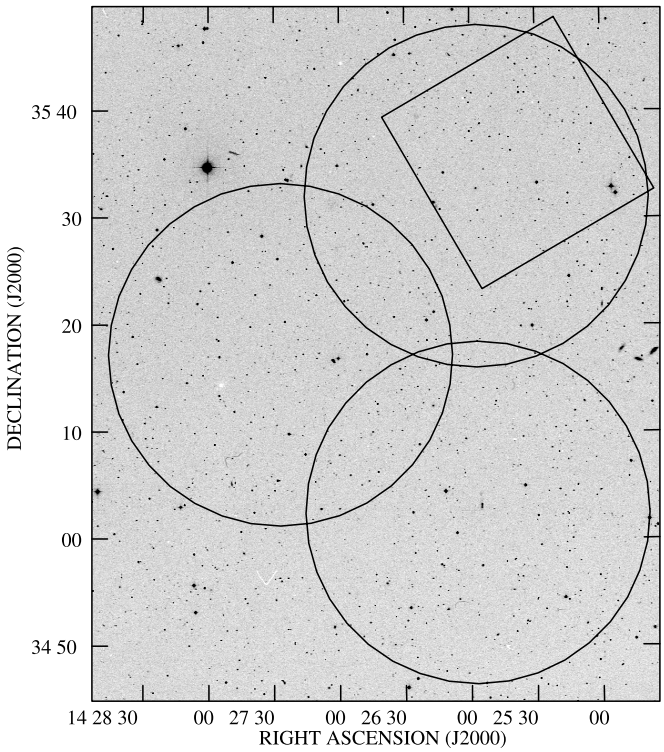

FIG. 1.—The survey fields. The circles represent the VLA primary beam FWHM (32′) for the three array pointings (north, east, and south), while the square represents the region observed with *Chandra* by Wang et al. (2004). These are superposed on a DPOSS gray-scale image.

2. RADIO OBSERVATIONS AND REDUCTION

We observed three overlapping fields within the NDWFS in Bootes with the VLA in the A configuration at 20 cm. These fields, labeled north, east, and south, are shown in Figure 1, which also depicts the *Chandra* survey field of Wang et al. (2004). The field center coordinates and other details of the observational setup are given in Table 1. The spectral line mode was used to minimize bandwidth smearing and facilitate the flagging of narrowband radio interference. The correlator was configured to provide two sets of seven channels (3.125 MHz separation), each centered at 1.3649 and 1.4351 GHz. Both left- and right-handed circular polarizations were measured at the two frequencies. Each field was observed in 40 minute blocks, interspaced with 2 minute observations of the nearby secondary calibrator 1416+347 ($S_{1.435\,\rm GHz} = 1.96 \pm 0.01$ Jy) to correct drifts in the antenna gains and phases. Flux and bandpass calibration were accomplished with longer observations of the primary flux calibrator 3C 48 ($S_{1.435\,\rm GHz} = 15.01 \pm 0.01$ Jy; Baars et al. 1977) made at the start of each night. On-source integrations totaling 5.5, 4.9, and 5.4 hr were achieved at the north, east, and south positions, respectively.

The visibilities were processed using routines in NRAO's Astronomical Imaging Processing System (AIPS) software package. A standard antenna based calibration was applied to each data set after excising a very small fraction of the data that was corrupted by radio interference. The routine IMAGR was used to map the primary beam with the correct w-phase terms (DO3DIMAG = 1). Images were made using a robust weighting parameter of 1.1, which improved the beam shape at the expense of an ~7% increase in noise. Radio sources from the FIRST catalog (Becker et al. 1995) that were located outside the primary beams yet

TABLE 1
VLA Observing Parameters

Parameter	Value		
Observing dates	2003 Jun 26, 27; July 27		
Array configuration	A		
Min/max baseline (km)	0.68/36.4		
Number of antennas	27		
Primary beam FWHM (arcmin)	31.5		
IF frequencies (GHz)	1.3649 and 1.4351		
Number of channels per IF	7		
Channel separation (MHz)	3.125		
Effective bandwidth (MHz)	43.750		
Phase and gain calibrator	1416+347		
Flux and bandpass calibrator	3C 48		
Synthesized beam FWHM (arcsec)[a]	1.4		
Field Centers	**North**	**East**	**South**
R.A. (J2000)	14 25 57.0	14 27 27.0	14 25 57.0
Decl. (J2000)	35 32 00.0	35 17 12.0	35 02 24.0
Time on source (hr):	5.5	4.9	5.4
Map rms (μJy beam^{-1})	14.8	15.5	15.6

Note.—Units of right ascension are hours, minutes, and seconds, and units of declination are degrees, arcminutes, and arcseconds.
[a] Robust weighting.

capable of contributing significant side lobes were also cleaned. Self-calibration was helpful in improving the antenna based calibration, particularly in the South field, which is dominated by a double-lobed radio source (87GB 142337.6+351136). After convolving to a common resolution of 1.″40 FWHM, the three final images were placed on a common grid and combined. The resulting rms at the three field centers is $\sim$15 μJy beam^{-1}, which is in good agreement with the expected noise levels using the array parameters listed in the VLA Observational Status Summary. Since we have imaged only three array pointings, significant variations in sensitivity exist across the survey field. Close to the field centers where the sensitivity is the highest we can detect point sources as faint as $\sim$80 μJy. However, the faintest point source we are capable of detecting throughout the entire survey is $\sim$200 μJy. For this reason we do not attempt to produce a radio source catalog that is complete to a given flux density limit. This does not affect our ability to calculate flux density ratios and limits for the radio, infrared, and X-ray sources. However, it will impact our estimates of surface densities.

3. SOURCE IDENTIFICATION AND MATCHING

We restricted our radio survey to where the sensitivity in the combined pointings exceeded 40% of the pointing centers, i.e., where the 1 σ noise is less than 37 μJy beam^{-1}. This corresponds to a total area of 0.5 deg^2. We used SExtractor (Bertin & Arnouts 1996) to identify radio sources in our survey rather than the AIPS routine SAD or its variants, even though SExtractor is more commonly used to find and catalog sources in optical images. This was because of the package's flexibility and our experience using it. After first smoothing the input radio image with a Gaussian profile matching the synthesized beam, SExtractor identified groups of at least five contiguous pixels, each exceeding the locally defined 2.5 σ background fluctuations. From this first cut of source identification, only those with a peak pixel value exceeding five times the local background rms were classified as source candidates. These were checked visually, and the small fraction found to be detections of residual sidelobes or radio source structure (e.g., hot spots in jets) were deleted from the catalog. A total of 392 sources satisfied these selection criteria, of which 377 are pointlike or marginally resolved. These objects are classified as "compact" objects in the radio source catalog. Flux densities were measured using the AIPS task IMFIT with the final primary beam corrected image. We determined fluxes for extended objects using the AIPS task BLSUM.[10]

We estimated the number of false detections in our survey by running SExtractor with the same settings on the radio image multiplied by -1. Assuming that the background noise is symmetric with respect to the mean, the number of sources detected in the reversed image should equal the number of false positives. Only three negative "sources" were found that were not associated with side lobes, and all of these were $<$5.5 times the local rms. As a check of this analysis, we calculated the number of independent beams in the radio survey and then estimated the number of $\geq$5 σ detections one would expect from random fluctuations. For 5×10^6 beams we expect only two spurious 5 σ detections and none at the 6 σ level. We therefore expect minimal contamination of our radio catalog by false sources, with two to three of the nearly 400 detections being spurious.

We compared the coordinates of the compact sources with the NDWFS optical catalog.[11] It was found that two-thirds of the radio sources had an optical counterpart within 0.″3. Because the great majority of these identifications are real, this value was taken as the 1 σ relative positional accuracy. Similarly, the measured 1 σ scatter in ΔR.A. and Δdecl. between the 24 μm sources and their nearest optical counterparts is 0.″3 for $F_{24\ \mu\mathrm{m}} \geq 0.75$ mJy. The positional accuracy was somewhat worse ($\sim$1″) for the MIPS sources near 0.3 mJy. The positional accuracy of the soft band

[10] The measured 20 cm fluxes, positions, major/minor axes and position angles (if compact), and optical magnitudes or upper limits will be made available as a text file at http://www.astro.cornell.edu/~jhigdon/files/vla_bootes/radio_cat.txt.
[11] Catalogs were derived using the third data release (DR3) version of the NDWFS optical images (B. T. Jannuzi et al. 2005, in preparation; see http://www.noao.edu/noao/noaodeep/).

TABLE 2

Optically Invisible Radio Sources in the Bootes Subregion

Radio ID	Source	$F_{20\ \mathrm{cm}}$[a] (μJy)	$F^{\mathrm{peak}}_{20\mathrm{cm}}$ (μJy)	$a \times b$ (arcsec)	ϕ (deg)	$F_{24\ \mu\mathrm{m}}$[b] (μJy)	q[c]	B_W[d]	R[d]	I[d]
9	J142822.75+351849.8	511 ± 62	128	3.5 × 2.7	70	...	<−0.26	>27.2	>25.3	>25.1
19	J142813.97+351136.6	565 ± 36	378	1.9 × 1.5	126	...	<−0.30	>27.1	>25.2	>24.5
22	J142810.60+350659.2	308 ± 42	125	1.7 × 1.5	128	...	<−0.04	>26.9	>24.9	>24.3
49	J142744.94+352616.5	565 ± 32	378	1.9 × 1.5	126	...	<−0.30	>27.2	>25.3	>25.0
52	J142740.39+350117.5	240 ± 38	148	2.2 × 1.4	137	...	<0.07	>26.9	>25.3	>24.2
79	J142713.75+352134.5	948 ± 37	602	2.1 × 1.5	137	...	<−0.53	>26.8	>25.2	>25.3
92	J142702.54+351215.2	239 ± 34	210	1.5 × 1.4	49	...	<0.07	>27.1	>25.6	>24.7
97	J142701.06+351949.3	396 ± 32	271	1.7 × 1.6	69	234 ± 44	−0.24 ± 0.21	>27.2	>25.8	>25.2
110	J142652.98+353351.1	177 ± 30	162	1.8 × 1.3	129	...	<0.20	>27.1	>26.1	>25.5
114	J142650.00+350711.0	372 ± 47	164	2.4 × 1.8	40	...	<−0.12	>26.8	>25.5	>25.0
156	J142632.14+353614.2	799 ± 59	262	2.9 × 2.0	164	...	<−0.46	>27.0	>26.0	>25.4
176	J142624.94+350614.6	249 ± 35	171	1.9 × 1.5	14	462 ± 44	0.27 ± 0.17	>27.0	>25.5	>24.7
182	J142623.40+345821.1	554 ± 39	352	2.1 × 1.6	100	...	<−0.30	>27.0	>25.7	>24.7
185	J142621.92+353114.7	327 ± 35	230	1.6 × 1.6	131	...	<−0.07	>27.0	>26.0	>25.2
208	J142613.81+353154.4	189 ± 33	145	1.6 × 1.5	76	...	<0.17	>27.0	>26.0	>25.3
209	J142613.53+352810.9	165 ± 31	77	2.0 × 1.4	12	...	<0.23	>27.0	>25.9	>25.3
232	J142605.13+350604.2	512 ± 18	404	1.6 × 1.5	88	...	<−0.26	>26.9	>25.1	>24.7
245	J142602.35+350907.9	244 ± 29	230	1.6 × 1.3	2	440 ± 52	0.26 ± 0.17	>26.9	>25.2	>24.8
278	J142551.58+351543.2	445 ± 70	118	2.6 × 2.3	178	...	<−0.20	>27.1	>25.8	>25.6
282	J142550.49+352935.4	155 ± 30	77	2.3 × 1.5	19	...	<0.26	>27.2	>26.0	>25.3
305	J142544.84+351702.2	777 ± 83	165	3.4 × 2.6	77	...	<−0.44	>26.9	>26.2	>25.2
313	J142543.00+353049.2	1165 ± 71	296	3.0 × 2.6	11	...	<−0.62	>27.1	>25.8	>25.2
323	J142537.12+345229.2	181 ± 35	126	1.7 × 1.3	20	...	<0.19	>27.1	>25.5	>25.0
346	J142528.98+352824.8	367 ± 36	205	2.0 × 1.7	21	...	<−0.12	>27.0	>26.1	>25.4
349	J142527.24+352649.7	241 ± 47	108	2.5 × 1.7	80	...	<0.07	>27.1	>25.9	>25.1
362	J142525.04+344913.2	6738 ± 69	1806	3.0 × 2.3	44	...	<−1.38	>27.0	>25.8	>24.9
363	J142524.84+352554.1	145 ± 38	90	2.1 × 1.5	38	328 ± 52	0.35 ± 0.31	>27.2	>25.9	>25.3
375	J142519.91+352417.8	847 ± 50	346	2.5 × 1.9	42	...	<−0.48	>26.9	>26.0	>25.4
380	J142516.19+350248.1	1906 ± 40	1070	2.0 × 1.7	79	...	<−3.83	>26.9	>25.5	>24.9
388	J142508.28+353901.9	180 ± 34	111	2.3 × 1.3	56	...	<0.19	>27.1	>26.0	>25.3
389	J142507.78+354210.4	302 ± 21	164	2.1 × 1.7	116	[e]	...	>26.9	>26.1	>25.3
393	J142506.41+353813.4	171 ± 14	112	2.2 × 1.4	125	[e]	...	>27.0	>25.8	>25.2
410	J142457.20+351620.5	875 ± 75	307	2.9 × 1.9	151	...	<−0.49	>27.0	>25.8	>25.3
430	J142445.36+353417.1	1410 ± 62	423	3.3 × 1.9	102	[e]	...	>27.0	>25.9	>25.2
434	J142444.01+351227.1	588 ± 47	262	3.1 × 1.4	75	[e]	...	>27.0	>25.5	>24.7
441	J142435.59+351046.2	1486 ± 59	484	2.7 × 2.2	11	[e]	...	>26.5	>25.1	>24.4

[a] Integrated 20 cm flux in microjanskys.
[b] Integrated 24 μm fluxes (or nondetection) at radio source position.
[c] Values given by $q = \log(F_{24\ \mu\mathrm{m}}/F_{20\ \mathrm{cm}})$.
[d] The B_W, R, and I limits (5 σ) calculated in 2″ diameter apertures centered on the OIRS positions. See § 4.1.
[e] These OIRSs are outside the MIPS 24 μm survey area.

X-ray sources listed in Table 1 of Wang et al. (2004) ranges from 0.″3 to 3.″5, but is typically 1″. We will adopt this as the X-ray source positional accuracy.

The identification of optically invisible radio sources was a two step process. First we correlated the positions of all 377 compact radio sources with the NDWFS B_W-, R-, and I-band catalogs, stipulating that OIRS candidates must not have a cataloged optical counterpart centered within a 1.″5 radius (5 σ). For the candidates passing this test, we inspected the NDWFS images at these positions to verify that no optical source was visible in any band. A small number of candidates without apparent optical counterparts but close to the edges of field galaxies were also rejected. This process yielded 36 OIRSs, which we list in Table 2. The identification of optically invisible X-ray sources was carried out in a similar manner, starting with the thirteen sources in Table 1 of Wang et al. (2004) with positional uncertainties less than 2″ that lack B_W, R, and I counterparts.

To determine if the OIRSs and OIXSs had infrared counterparts, we then compared their positions with the MIPS 24 μm catalog ($F_{24\ \mu\mathrm{m}} \geq 0.3$ mJy), calling a radio and infrared source matched if their positions differed by less than 2.″5. Infrared fluxes or upper limits for the OIRSs are given in Table 2. Similarly, we adopted as criteria for matching radio to X-ray and X-ray to infrared sources that their coordinates agree to <2″.

4. RESULTS AND ANALYSIS

4.1. *Properties of the OIRS Population*

We identified a total of thirty-six OIRSs over the 0.5 deg^2 survey area, a number representing 10% of the total compact radio source population. Table 2 lists their radio catalog number, source name incorporating J2000 coordinates, and physical properties. Nearly all (86%) are detected above the 5.5 σ level, where we expect no spurious sources. Figure 2 shows 12″ × 12″ subimages from the NDWFS B_W, R, and I data centered on five of the OIRSs, along with the corresponding subimages from the MIPS 24 μm survey field. The radio continuum source structure for each is shown contoured on the I-band subimages, with the

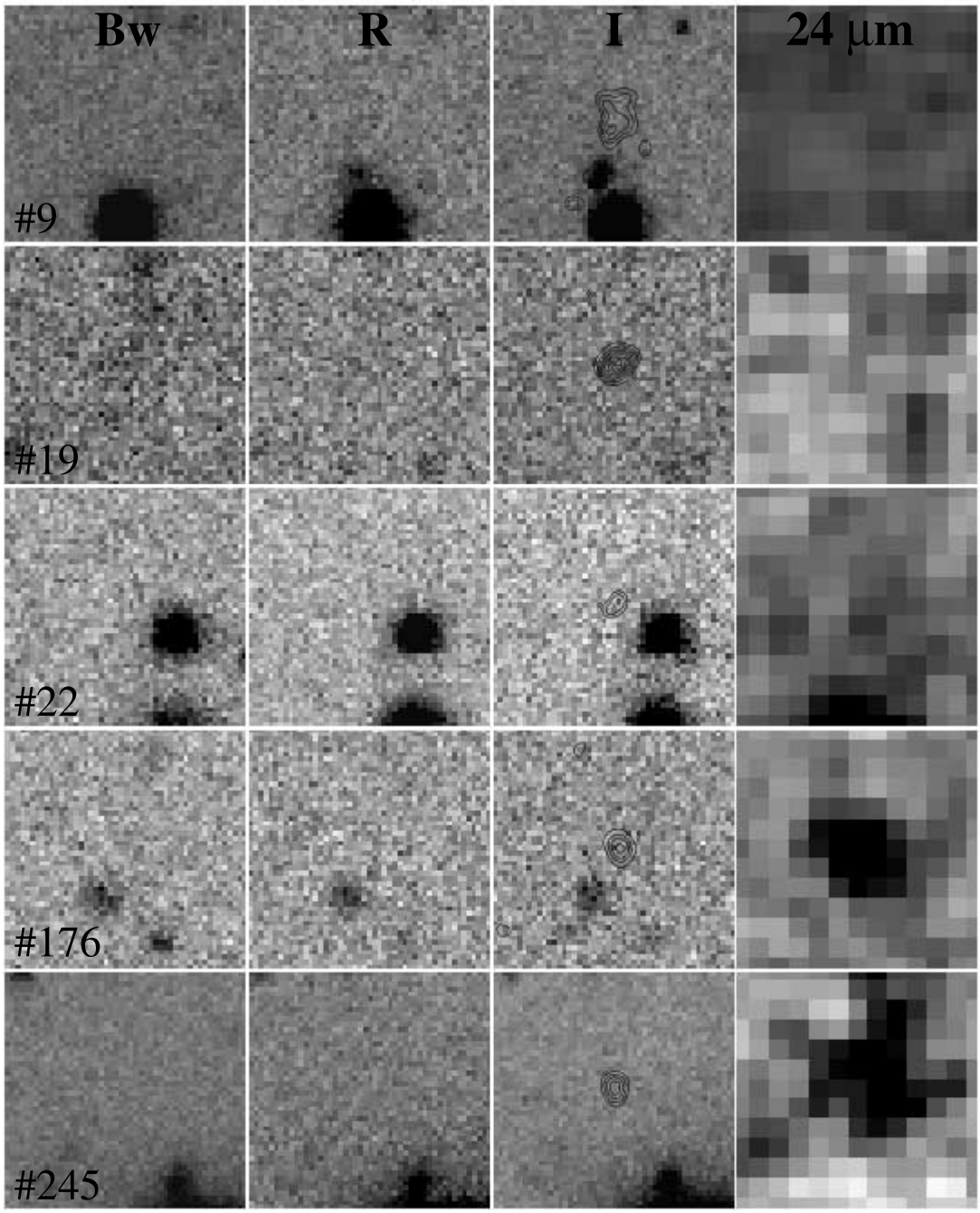

FIG. 2.—Sample of five optically invisible radio sources (OIRSs) shown in optical B_W, R, I, and MIPS 24 μm bands. Radio contours are shown superposed on the I image, with the lowest contour representing the local 3 σ level. Each field is $12'' \times 12''$.

lowest contour representing the local 3 σ noise level in the radio image.

The precise magnitude limit for an OIRS depends on the position of the source in the NDWFS field. We therefore derived B_W, R, and I upper limits for the 31 OIRSs within $2''$ diameter apertures centered on their positions using the appropriate NDWFS zero-point constants.[12] Typical magnitude limits are 27.0, 25.7, and 25.0 (Vega) in B_W, R, and I, respectively. These are listed in Table 2 for each source. Figure 3 shows a histogram of the integrated 20 cm continuum flux densities for the OIRS sample. Nearly 90% are submillijansky radio sources (median $F^{\rm total}_{20\ {\rm cm}} = 0.40$ mJy), though five have flux densities greater than 1 mJy. Source 362 possesses the peak flux density for the sample of nearly 7 mJy. Thirty-one OIRSs were included within the MIPS survey area. Only four of these—sources 97, 176, 245, and 363 in Table 2—were detected at 24 μm above 5 σ. We stack-averaged the remaining 27 MIPS subimages in an attempt to detect fainter emission levels. No significant signal was detected, and we set an upper limit on the average infrared flux density for the ensemble of $F_{24\ \mu{\rm m}} < 60$ μJy (5 σ).

The small number of radio/infrared matches (13%) is a significant result, since from the surface densities of the 20 cm and 24 μm sources, we estimate the probability of a random match to be less than 1%. We verified the lack of overlap between these

[12] Limits were calculated using $q_0 - 2.5 \log[5 \times {\rm rms} \times (N_{\rm pix})^{1/2}]$, where $N_{\rm pix}$ and rms are the number of pixels and variance within the $2''$ diameter aperture respectively, and q_0 is the zero-point constant.

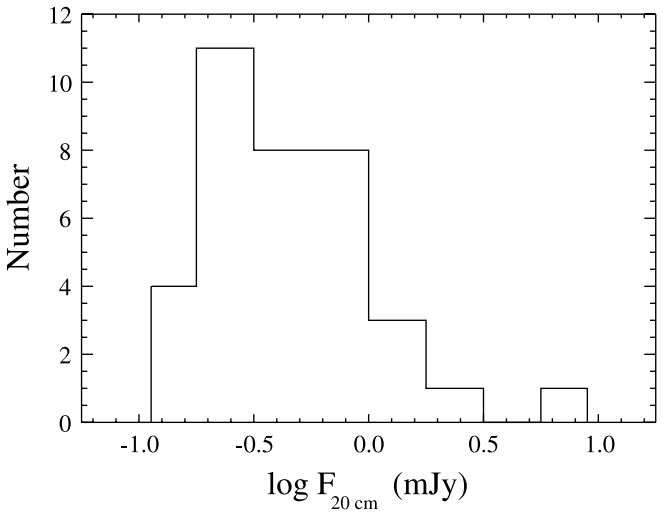

FIG. 3.—Histogram of 20 cm flux densities for the OIRS sample.

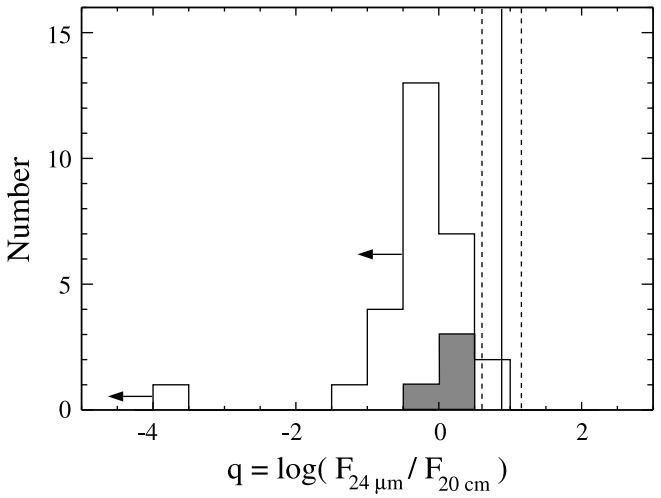

FIG. 4.—Distribution of q for the OIRS sample. The shaded histogram represents the four OIRS detected at 24 μm by MIPS. The unshaded histogram represents upper limits for q calculated using $F_{24\,\mu m} < 0.3$ mJy. The vertical solid and dashed lines represent, respectively, the mean value and range for q in $z \lesssim 2$ starburst-dominated systems as determined by Appleton et al. (2004).

two source populations by plotting the OIRS positions on the MIPS 24 μm image and inspecting the result visually. Two of these MIPS-detected sources are shown in the bottom two rows of Figure 2. Eight OIRSs are situated in the survey area covered by both *Chandra* and MIPS (0.08 deg^2). None was detected at 24 μm or in any of the X-ray bands. This sets upper limits of 0.3 mJy at 24 μm and 1.5×10^{-16} ergs s^{-1} cm^{-2} in the 0.5–2.0 keV X-ray band for this subsample.

Because of the variable sensitivity throughout the radio images, simply dividing the number of OIRSs by the survey area would lead to an underestimate of their true surface density ($\sigma_{\rm OIRS}$). This is due to the fact that the fainter radio sources can only be detected near the pointing centers where the sensitivity is the highest. We have attempted a first-order correction to this effect by first weighting each OIRS by the ratio of the total survey area to the area where it could have been detected given its peak 20 cm flux density (Hopkins et al. 1999). Doing so resulted in an average surface density of $\sigma_{\rm OIRS} = 104 \pm 17$ deg^{-2}, where the uncertainty represents Poisson counting errors only. There is a strong dependence on flux density. We divided the OIRSs into three flux density bins, $F^{\rm peak}_{20\,\rm cm} < 400$ (17 sources), 400–600 (13 sources), and >600 (6 sources) μJy beam^{-1}, and calculated the average surface density for each as above. We find that $\sigma_{\rm OIRS}(<400\ \mu{\rm Jy\ beam^{-1}}) = 66 \pm 12$ deg^{-2}, $\sigma_{\rm OIRS}(400$–$600\ \mu{\rm Jy\ beam^{-1}}) = 26 \pm 11$ deg^{-2}, and $\sigma_{\rm OIRS}(>600\ \mu{\rm Jy\ beam^{-1}}) = 12 \pm 5$ deg^{-2}, i.e., the OIRS surface density increases with decreasing 20 cm flux density.

4.2. *Are the OIRSs Powered by Star Formation or AGNs?*

The logarithm of the infrared to radio continuum flux density ratio, or q, is a useful parameter for distinguishing sources powered by massive star formation from AGNs, and especially radio-loud AGNs. In Figure 4 we show the distribution of q using the MIPS 24 μm and 20 cm radio continuum data in Table 2 for the OIRS sample [i.e., $q = \log(F_{24\,\mu m}/F_{20\,\rm cm})$]. The four OIRSs detected by MIPS are represented by the shaded histogram bins ($-0.5 \le q \le 0.5$). For the 27 other OIRSs we show a histogram of upper limits for q, using $F_{24\,\mu m} = 0.3$ mJy in the calculation. The small number of sources precludes a strong conclusion statistically, but we note that three of the four OIRSs with MIPS detections have positive values of q, with a mean of 0.29. Only source 97 has a negative q. On the other hand, of the 27 OIRSs not detected by MIPS, two-thirds (18 of 27) have negative q values. Since these are all upper limits, it is likely that even a larger fraction of these sources will have $q < 0$.

We first considered the origin of the OIRSs' emission by comparing the values and upper limits of q in Table 2 to those derived from local starbursts and AGNs for a range of redshifts. Using the most luminous galaxy ($3 \times 10^{12}\ L_\odot$) spectral energy distribution (SED) from Lagache et al. (2003), we calculated the observer's frame $F_{850\,\mu m}/F_{24\,\mu m}$ ratio for redshifts of 1, 2, and 3. This in turn was used with the scaling in Chary & Elbaz (2001) to calculate the corresponding 20 cm flux densities. Under these assumptions, starburst galaxies with 20 cm flux densities of 200 μJy should have 24 μm flux density of 2.8 mJy at $z = 1$, 2.4 mJy at $z = 2$, and 1.6 mJy at $z = 3$. In short, starbursts detected in our radio survey would be easily detected in our 24 μm data. These will in turn give rise to values of $q = 1.15$, 1.08, and 0.90 for starbursts at these three redshifts. This is in agreement with Appleton et al. (2004), who found that for flux densities measured at 24 μm and 20 cm, starburst-dominated systems have $q = 0.8 \pm 0.3$ for $z \lesssim 2$. This range is represented in Figure 4 as the solid and dashed vertical lines. The values of q for starburst-dominated systems are substantially greater than the upper limits shown, and even appear significantly larger than the q-values determined for the four OIRSs detected by MIPS. Thus, for virtually the entire OIRS sample a clear enhancement in radio continuum emission over that expected for a pure starburst is evident. This indicates the presence of a dominant AGN component.

A more detailed illustration with a broader range of SED types is presented in Figure 5, where q is plotted against the logarithm of 20 cm flux density. Four families of curves are shown, representing (*top to bottom*) (1) a normal Sc galaxy with a SFR of 3 $M_\odot$ yr^{-1}, (2) a high-luminosity starburst/ULIRG with a 3000 $M_\odot$ yr^{-1} SFR, (3) a type 2 Seyfert AGN (NGC 262), and (4) a QSO with 3C 273's SED. The late spiral, ULIRG, and AGN/Seyfert SEDs were taken from the compilation of Xu et al. (2001), while the 3C 273 SED was taken from the NED online database. For the two star-forming galaxy templates, we first calculated the rest-frame 20 cm luminosity ($L_{20\,\rm cm}$ in W Hz^{-1}) for a given star formation rate (in $M_\odot$ yr^{-1}) using the calibration given in equation (6) of Bell (2003). Using this value and the SED, we derived the observer-frame $F_{24\,\mu m}/F_{20\,\rm cm}$ ratio as a function of

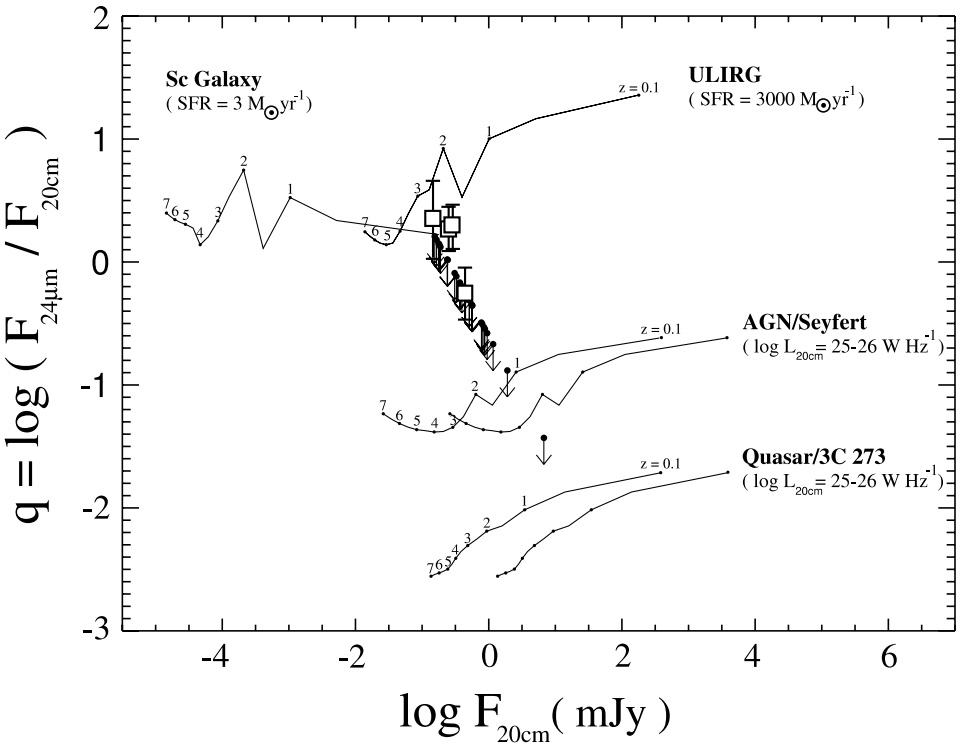

FIG. 5.—Infrared-radio color-magnitude diagram. The four sets of tracks show the expected infrared-to-radio flux density ratio vs. radio flux density for various SEDs as a function of redshift. *Top to bottom*: An SFR = 3 $M_\odot$ yr^{-1} late spiral, an SFR = 3000 $M_\odot$ yr^{-1} ULIRG, a Seyfert AGN with 20 cm luminosities of 10^{25} and 10^{26} W Hz^{-1}, and a quasar with 3C 273's SED and 20 cm luminosities identical to that of the Seyfert galaxy. Redshift is indicated along the tracks. The open squares represent the four OIRSs detected at 24 μm. The filled circles with arrows are upper limits for the remaining 27 OIRS not detected by MIPS.

redshift from $z = 0.1$–7.0. We next calculated the observer-frame 20 cm flux density ($F_{20\,\mathrm{cm}}$, in μJy) for these redshifts using

$$L_{20\,\mathrm{cm}} = 1.26 \times 10^{-35} F_{20\,\mathrm{cm}} d_L^2 (1+z)^{\alpha-1}\ (\mathrm{W\ Hz^{-1}}), \quad (1)$$

where d_L is the luminosity distance in centimeters. The radio spectral index α (where $F_\lambda \propto \lambda^\alpha$) was derived from the SED templates over the wavelength range 7 to 20 cm. The starburst, normal, and AGN templates gave similar average spectral indices (mean $\alpha = 0.65$). For the two AGNs we considered 20 cm luminosities of 10^{25} and 10^{26} W Hz^{-1} and calculated observer-frame $F_{24\,\mu\mathrm{m}}/F_{20\,\mathrm{cm}}$ ratios and 20 cm flux densities as above, also for the redshift range $z = 0.1$–7.0. The resulting four sets of tracks are indexed by redshift from $z = 0.1$ to 7.

The four MIPS-detected OIRSs are shown as open squares in Figure 5. For three (176, 245, and 363), their positions are consistent with the SFR = 3000 $M_\odot$ yr^{-1} ULIRG template over a $z = 2$–3 redshift range, albeit somewhat displaced below the track. Note that increasing/decreasing the SFR for either the ULIRG or Sc galaxy templates has the effect of moving the tracks to the right/left. The vertical position is controlled solely by the shape of the SED and redshift. It is therefore possible that these could be at $z = 4$–7 if of sufficient luminosity. The other MIPS-detected OIRS (97) is situated well below the ULIRG track, with $q = -0.24 \pm 0.21$. The remaining 27 OIRSs with q upper limits are shown as filled circles with arrows. Again, two-thirds of them have negative values of q, which is inconsistent with late spiral or ULIRG SEDs at any redshift. These sources show a clear excess in radio emission relative to the infrared compared to a system powered by star formation. The q upper limits cannot be used to distinguish between Seyfert and quasar templates in Figure 5 (both require $q \lesssim -1$ for all z). However, it is clear that the bulk of the OIRSs are powered primarily by an AGN, with many being radio-loud.

4.3. *Are the OIXSs Starbursts or AGN-Powered Systems?*

X-ray sources with very faint optical counterparts or no counterparts at all are also found in deep surveys (e.g., Barger et al. 2003). Like the optically faint radio source population, these objects have been proposed to represent highly obscured starburst galaxies or AGNs at very high redshift, or possibly even AGNs that are overluminous in X-rays compared to local examples. To investigate the nature of these sources, we examined the 11 X-ray sources in Table 1 of Wang et al. (2004) without the B_W, R, and I counterparts observed by MIPS at 24 μm. The properties of these OIXSs, including source number (taken from Table 1 in Wang et al. 2004), J2000 coordinates, soft-band X-ray fluxes or upper limits, and optical limits, are given in Table 3. Also listed are the OIXSs' X-ray "hardness ratio" (HR), defined as HR = $(H - S)/(H + S)$, where H and S represent the hard 2–7 keV and soft 0.5–2 keV band counts, respectively.

No OIXSs were detected at 24 μm. This has important consequences for the origin of their X-ray luminosity. Weedman et al. (2004) used infrared and X-ray spectra from a sample of nine starburst regions in four merging systems and three obscured AGNs to determine empirically that the ratio IR/X (defined to be the 24 μm flux density in millijanskys to the *Chandra* 0.5–2.0 keV flux in units of 10^{-16} ergs s^{-1} cm^{-2}) has a lower bound of 0.2 for starbursts and obscured AGNs for $z \leq 3$. Ratios of IR/X smaller than 0.2 indicate that the source is powered by a relatively unobscured AGN. Note that we should detect any soft-band X-ray source in Wang et al.'s (2004) survey that is powered by a starburst or heavily obscured AGN (i.e., IR/X > 0.2) given the *Chandra* and MIPS 24 μm sensitivities. This empirical criterion can be used to classify the seven OIXSs in our MIPS survey

TABLE 3
OPTICALLY INVISIBLE X-RAY SOURCES

X-Ray ID No.[a]	Source	$F_{0.5-2\ \mathrm{keV}}$[b]	HR[c]	IR/X[d]	B_W[e]	R[e]	I[e]
9	J142539.55+353357.9	6.9	$-0.43^{+0.19}_{-0.17}$	<0.04	>26.8	>25.9	>25.3
15	J142530.71+353911.3	11.9	$0.12^{+0.11}_{-0.11}$	<0.03	>27.1	>25.8	>25.4
31	J142555.40+353650.4	3.3	$-0.56^{+0.33}_{-0.25}$	<0.08	>26.9	>25.8	>25.3
51	J142546.33+353349.4	<1.5[f]	>0.56	...	>27.0	>26.0	>25.3
69	J142531.17+353921.6	<1.5[f]	>0.73	...	>26.9	>26.2	>25.3
70	J142530.63+353420.3	9.4	$-0.42^{+0.16}_{-0.14}$	<0.03	>27.0	>25.9	>25.3
73	J142526.68+353140.8	7.0	$-0.13^{+0.19}_{-0.18}$	<0.04	>27.0	>26.0	>25.3
96	J142558.13+353216.1	3.8	$-0.33^{+0.30}_{-0.26}$	<0.08	>26.9	>25.8	>25.3
103	J142544.20+354018.4	<1.5[f]	>0.86	...	>26.9	>25.9	>25.4
112	J142527.59+354012.1	3.2	$0.10^{+0.25}_{-0.26}$	<0.09	>27.1	>25.8	>25.2
120	J142522.40+353517.2	<1.5[f]	>0.40	...	>26.9	>25.8	>25.2

[a] X-ray source number from Table 1 in Wang et al. (2004).
[b] Integrated soft (0.5–2.0 keV) band flux in units of 10^{-16} ergs s^{-1} cm^{-2} from Wang et al. (2004).
[c] X-ray hardness ratio from Wang et al. (2004). HR = $(H - S)/(H + S)$, where H and S are the hard (2–7 keV) and soft (0.5–2 keV) band counts.
[d] The 24 μm to soft X-ray flux radio, in units of mJy/(10^{-16} ergs s^{-1} cm^{-2}).
[e] B_W, R, and I limits (5 σ) calculated in 2″ diameter apertures centered on the OIXS positions, as in § 4.1.
[f] OIXSs 51, 69, 103, and 120 were only detected in the *Chandra* hard or "total" bands and not the 0.5–2 keV soft band. Their positional accuracies are all <1″.

that were detected in the soft X-ray band. Figure 6 shows a plot of IR/X versus the X-ray hardness ratio for these sources. All seven have values of IR/X < 0.2, which clearly indicates the presence of a dominant unobscured AGN. We cannot classify the four OIXSs in Table 3 with soft-band upper limits. Nevertheless, at least 64% (7/11) of the OIXSs are powered by unobscured AGNs.

The X-ray hardness ratio can be used to place rough constraints on the redshift distribution of the OIXSs. Wang et al. (2004) argued that the X-ray spectrum softens with increasing redshift, with HR < 0.6 marking $z \gtrsim 1$ objects. In support of this, Wang et al. (2004) determined photometric redshifts for five X-ray sources detected at I and z' bands but not in R. The three with $z_{\mathrm{phot}} \sim 1$–2 have hardness ratios between −0.1 and 0.6, while the two softest sources (HR $\lesssim -0.5$) have $z_{\mathrm{phot}} \sim 4.3$. By this criteria, 9 out of the 11 OIXSs in our sample can have $z > 1$ (HR < 0.6). Four can possibly at $z \sim 4$–5 (HR < −0.5).

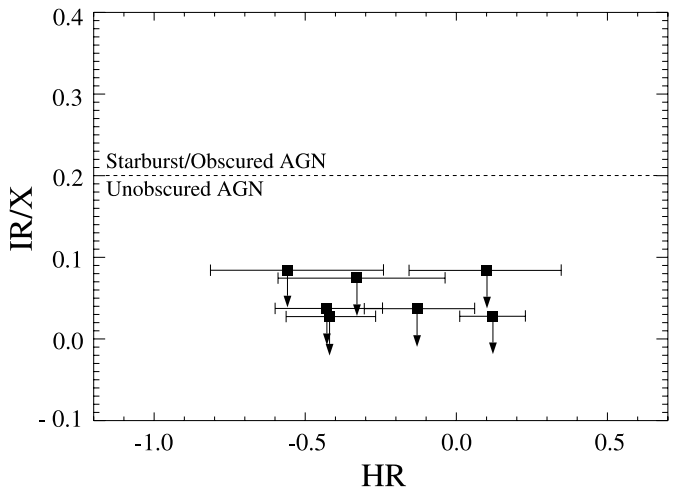

FIG. 6.—Infrared to X-ray ratio (IR/X) vs. the X-ray hardness ratio (HR) for the seven optically invisible X-ray sources detected in the *Chandra* soft 0.5–2 keV band. The dashed line marks IR/X = 0.2, which separates starburst- and obscured AGN–powered emission (IR/X > 0.2) from systems dominated by unobscured AGNs (IR/X < 0.2).

No OIXSs were detected by our radio survey, which sets a 20 cm flux density limit of ~200 μJy for these sources. Note that at these levels we would have easily detected radio-loud quasars with 3C 273–like SEDs and 20 cm luminosities greater than 10^{25} W Hz^{-1} beyond redshifts of 6 (Fig. 5), and most Seyfert systems with similar 20 cm luminosities. OIXSs thus appear to be largely a population of radio-quiet AGNs.

4.4. *Comparison of Radio, Infrared, and X-Ray Source Catalogs*

This study is concerned primarily with the optically invisible source populations. However, it is worthwhile considering the characteristics of the radio, infrared, and X-ray populations as a whole. Because of the tight correlation between infrared and radio flux densities for infrared-luminous galaxies (de Jong et al. 1985; Helou et al. 1985) and because of the indications that the submillijansky radio population corresponds to faint, star-forming galaxies (e.g., Haarsma et al. 2000), a strong overlap between the radio and MIPS survey samples might be expected. Such an overlap is implied by the results displayed from analogous work in the First Look Survey (FLS) area, for which Appleton et al. (2004) show a clear correlation between flux densities at 24 μm and at 20 cm (see their Fig. 2). However, the sources plotted there are only those detected in both infrared and radio with redshifts less than ~2, which does not provide a comparison of the entire radio and infrared samples in the FLS survey region.

Table 4 shows various source detection statistics for our radio, infrared, and X-ray survey regions. First, we note that our radio survey does not go sufficiently deep to detect the majority of MIPS sources. Within the 0.5 deg^2 VLA survey area there are 1405 MIPS detections, and 377 compact radio sources. Only 125 are detected in both wavebands. That is, 9% ± 1% of the infrared sources have radio counterparts and 33% ± 3% of the radio sources have MIPS counterparts with fluxes of at least 0.3 mJy. This is not too surprising, since our radio observations were intended to detect the $F_{24\ \mu\mathrm{m}} \geq 0.75$ mJy source population. There are 216 such 24 μm sources in our survey area. Only 33% ± 5% of these have radio counterparts. Similarly, 23% ± 3% of the compact radio sources have infrared counterparts >0.75 mJy at 24 μm. Sensitivity variations will of course introduce a bias

TABLE 4
SOURCE DETECTION STATISTICS IN RADIO AND X-RAY SURVEYS

Parameter	Total Number	σ[a]	MIPS[b] (%)	Radio[c] (%)	X-Ray[d] (%)
Radio Survey					
MIPS sources (>0.3 mJy)	1405	2810 ± 75	...	9	
Compact radio sources	377	754 ± 39	33	...	
OIRSs	36	104 ± 17[e]	13[f]	...	
X-Ray					
X-ray sources	104[g]	1486 ± 146	17	11	...
MIPS sources (>0.3 mJy)	240	3429 ± 221	...	11	8
Compact radio sources	73	1043 ± 123	36	...	14
OIXSs	11	157 ± 47	0	0	...
OIRSs	8	114 ± 40	13	...	0

[a] Average surface density in square degrees.
[b] Percentage of sources detected at 24 μm by MIPS.
[c] Percentage of sources detected at 20 cm.
[d] Percentage of sources detected in *Chandra* 0.5–2.0 keV band by Wang et al. (2004).
[e] Surface density for all 36 OIRSs, including those outside the MIPS survey area.
[f] Percentage of the 31 OIRSs observed by MIPS that were detected at 24 μm.
[g] Number of X-ray sources observed by MIPS at 24 μm.

against detecting faint radio sources far away from the three pointing centers. However, we do not see a large effect. If we restrict ourselves to regions in which the radio rms is less than 17 μJy beam^{-1}, i.e., an area of 0.17 deg^2, we find similar detection fractions: 32% ± 7% (25/78) of the $F_{24\,\mu m} \geq 0.75$ mJy sources have radio counterparts, while 19% ± 4% (25/130) of the compact radio sources MIPS counterparts with $F_{24\,\mu m} \geq 0.75$ mJy. This shows that greater 20 cm sensitivities are required to detect the bulk of the infrared sources for which IRS spectra can be obtained in reasonable integration times.

When comparing the radio and infrared populations, it is therefore important to realize that only a relatively small fraction of sources are detected in both bands. This is illustrated in Figure 7,

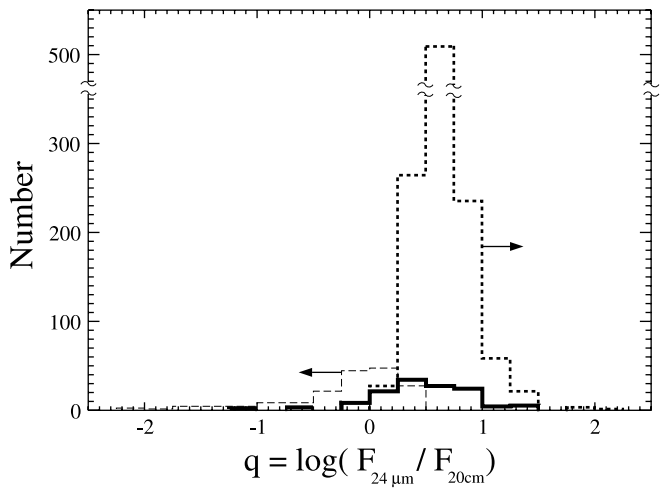

FIG. 7.—Distribution of q for the full radio and infrared sample. The thick solid-line histogram depicts q for the 125 sources detected at both 24 μm and 20 cm. The thick-dashed line histogram shows q lower limits for the 1086 sources detected only in the infrared, where the $F_{20\,cm}$ upper limit was taken to be a point source with 5 times the rms at the source position in the final radio image. All sources in the histogram lie within or to the right of the bins shown. The thin-dashed line histogram shows the 194 radio sources not detected by MIPS, assuming a 24 μm flux upper limit of 0.3 mJy. Similarly, the sources in this histogram will lie within or to the left of the bins indicated.

which shows histograms of q for the 125 sources detected at both 24 μm and 20 cm (*thick solid line*), the 194 radio sources not detected at 24 μm (*thin dashed line*), and the 1086 24 μm sources with no measured radio fluxes (*thick dashed line*). For the radio-only sample we calculated q upper limits using $F_{24\,\mu m} = 0.3$ mJy. For the infrared-only–detected sample we calculated lower limits for q by setting $F_{20\,cm}$ equal to that of a point source with a peak flux density 5 times the radio image rms at the infrared source's position.

The sources detected at both 24 μm and 20 cm show a distribution of q that peaks at ~0.5. This is in reasonable agreement with Appleton et al.'s (2004) result, that $q = 0.8 \pm 0.3$ for the radio-infrared correlation at $z \lesssim 2$. The smaller range of q evident in Figure 7 may be partly due to the detection of $z > 2$ ULIRGS, which will have progressively smaller q with increasing redshift (see the ULIRG track in Fig. 5). This is consistent with a population of galaxies powered primarily by star formation, though an AGN contribution is still possible. Radio-loud AGNs are certainly apparent in the negative q tail. AGNs also clearly dominate the population of radio sources with no MIPS detections in Figure 7. However, the bulk of the infrared sources in the radio survey field have only lower limits for q, with a strong peak between 0.5 and 1. While this is consistent with star formation being the dominant power source, deeper 20 cm observations are required to measure q and quantify the radio-infrared correlation for the majority of galaxies in the survey. Figure 7 suggests that the radio- and infrared-selected populations do not overlap, i.e., that each represents populations of AGN- and starburst-dominated galaxies, respectively. Higher sensitivity radio and infrared observations are needed to verify this.

An important related question is whether the OIRSs represent a population significantly different from the radio sources with optical counterparts, whose characteristics (e.g., starburst or AGN dominated) can be determined through optical or near-infrared spectroscopy. There is a qualitative indication that this might be so from the overall difference in the infrared detection rate for radio sources in the OIRS sample compared to the full radio sample. We find that 33% ± 3% of the compact radio sources in the entire sample are detected in the infrared to the 5 σ sensitivity

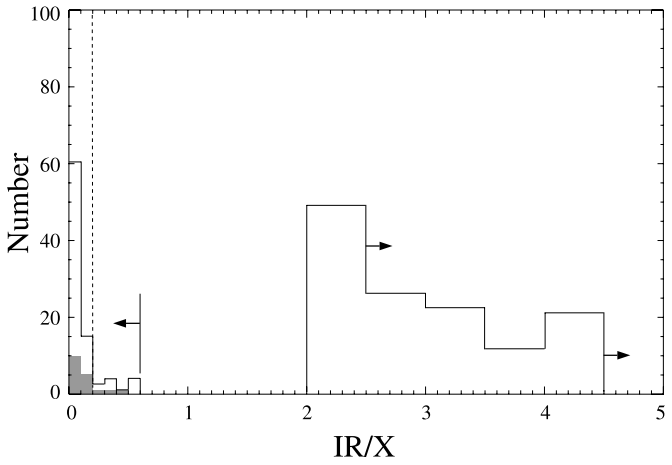

FIG. 8.—Distribution of IR/X for the full sample of infrared and X-ray sources in the overlapping survey area. The shaded histogram shows values of IR/X for the 18 objects detected in both MIPS 24 μm and *Chandra* 0.5–2 keV band emission. The unshaded histograms show upper and lower limits to IR/X for the *Chandra*-only (*left histogram*) and MIPS-only (*right histogram*) detected samples, respectively. Sources with IR/X > 0.2 are consistent with starbursts or heavily obscured AGNs, which includes all MIPS-only sources. Sources with IR/X < 0.2 have their luminosity dominated by an relatively unobscured AGN. This encompasses most *Chandra*-only sources.

limit, whereas only 13% $\pm$ 7% of the OIRSs are detected. Here the uncertainties represent Poisson statistics only. While this suggests a difference in the two radio populations, the small number of sources in the OIRS sample prevents this from being a statistically robust conclusion.

In the portion of the field covered by both the *Chandra* and *Spitzer* surveys ($\sim$0.07 deg^2), there are 240 24 μm sources brighter than 0.3 mJy (see Table 4) and 104 *Chandra* soft-band sources brighter than 1.5×10^{-16} ergs s^{-1} cm^{-2}. Only 18 sources are detected in both infrared and X-ray bands for which IR/X can be determined directly. A comparison of these sources is shown in Figure 8. For the 18 sources detected in both bands (*shaded histogram*), nearly all (80%) have IR/X ≤ 0.2, indicating a relatively unobscured AGN. For sources detected by *Chandra* but not MIPS, IR/X upper limits were determined as 0.3 mJy/($F_{0.5-2.0\,\mathrm{keV}}$) with the soft X-ray flux in units of 10^{-16} ergs s^{-1} cm^{-2}. For sources detected only at 24 μm, we calculated lower limits to IR/X using $F_{24\,\mu\mathrm{m}}$ in millijanskys divided by 1.5. Figure 8 shows a clear separation between the sources detected only by MIPS or *Chandra*, with the former being identified with starburst- or obscured AGN–dominated systems and the latter with unobscured AGNs. Quantitatively, 90% of the *Chandra*-only detections have IR/X < 0.2. Similarly, 90% of the MIPS-only detections have IR/X > 0.2. These results apply to the full sample of sources in the overlapping area, virtually all of which have optical identifications, and indicate that the great majority of X-ray sources are powered by AGNs.

5. DISCUSSION

5.1. *Space Densities of the OIRS and OIXS Populations*

We, of course, have no direct measure of the redshifts for the OIRS population. However the requirement that they be optically invisible likely forces the majority to be at $z \gtrsim 1$. Supporting evidence for this comes from IRS spectroscopy of a sample of 16 optically faint and invisible MIPS sources in Bootes with $F_{24\,\mu\mathrm{m}} \geq 0.75$ mJy in Houck et al. (2005). For the 10 optically invisible infrared sources, the median spectroscopic redshift was 2.1, with only one object having a redshift less than 1, and that at $z = 0.7 \pm 0.1$. We can calculate rough estimates of the OIRS space density by assuming that they lie within certain broad redshift ranges. By comparing these with measured or estimated space densities of other extragalactic objects (see Table 5) we can gain additional clues into their nature. Arguments based on surface density comparisons are subject to various complexities and assumptions (i.e., the OIRS redshift range) that are difficult to take into account. Nevertheless, such an approach is still informative.

The average surface density of the 27 OIRSs with no MIPS detections, sources whose emission is likely to be dominated by an AGN, is $\sigma_{\mathrm{OIRS}} = 80 \pm 15$ deg^{-2}. For our adopted flat ΛCDM cosmology and H_0, this corresponds to a mean space density $\rho_{\mathrm{OIRS}} = (2.4 \pm 0.5) \times 10^{-6}$ Mpc^{-3} over a $1 < z < 5$ redshift range. This is much smaller than the space density of current day massive ellipticals ($\rho_{\mathrm{elliptical}} \sim 10^{-3}$ Mpc^{-3}; Marzke et al. 1994), though comparable to that of local radio galaxies ($\rho_{\mathrm{RG}} \sim 10^{-6}$ Mpc^{-3}; Osterbrock 1989).

This can also be compared with the space density of bright ($M_B < -26$) quasars over $0.4 < z < 5$ shown in Figure 3 of Fan et al. (2001), which combines results from Two Degree Field (2dF; Boyle et al. 2000), Warren et al. (1994), and Schmidt et al. (1995), as well as the Sloan Digital Sky Survey (SDSS). The OIRS space density is considerably larger than that of bright optically selected quasars, even at $z \sim 2.5$ where the quasar distribution peaks ($\rho_{\mathrm{qso}} \sim 5 \times 10^{-7}$ Mpc^{-3}). The discrepancy is much larger at lower and higher redshifts. For example, from $z = 3$–5 the bright quasar space density drops from $\sim 2 \times 10^{-7}$ to

TABLE 5
AVERAGE SPACE DENSITY COMPARISON

Objects	ρ (10^{-6} Mpc^3)	Redshift	Notes
OIRS	3.1 $\pm$ 0.5	$1 < z < 5$	Calculated using all 36 OIRSs in the VLA survey
	2.4 $\pm$ 0.5	$1 < z < 5$	Calculated using the 27 OIRSs not detected by MIPS
	4.1 $\pm$ 0.8	$1 < z < 3$	
OIXS	4.7 $\pm$ 1.4	$1 < z < 5$	Calculated using all 11 OIXSs in *Chandra* survey
	3.9 $\pm$ 1.3	$1 < z < 5$	Calculated using the nine OIXSs with HR < 0.6
	3.3 $\pm$ 1.5	$1 < z < 3$	Calculated using the five OIXSs with $-0.5 <$ HR < 0.6
Ellipticals	10^3	$\sim$0	Local massive ellipticals (Marzke et al. 1994)
Radio galaxies	$\sim$1	$\sim$0	Local radio galaxies (Osterbrock 1989)
Submillimeter sources	70	$1 < z < 3$	$F_{850\,\mu\mathrm{m}} > 2.2$ mJy (Barger et al. 1999)
Bright QSOs	0.01	$z = 1$	$M_B < -26$ QSOs; from Fig. 3 in Fan et al. (2001)
	0.5–0.01	$2 < z < 5$	$M_B < -26$ QSOs; from Fig. 3 in Fan et al. (2001)
Faint QSOs	30–3	$3 < z < 5$	$-23 < M_B < -22$ QSOs; extrapolated from Fan et al. (2001)

$\sim 1 \times 10^{-8}$ Mpc^{-3}, which is smaller than the OIRS space density by 1 and 2 orders of magnitude, respectively.

However, the OIRSs are almost certainly less luminous optically than $M_B = -26$. Assuming a power-law form for the optical continuum of $f_\nu \propto \nu^{-0.5}$, the B_W upper limit of $\sim$26.5 implies absolute magnitude upper limits of approximately $M_B = -18$ to -23 for $z = 1$–5. These values are less than or equal to $M_B = -23$, the traditional boundary between Seyfert galaxies and quasars. The cumulative luminosity function for optically selected quasars at $z > 3.6$ in Fan et al. (2001) is

$$\log \Phi(z, < M_B) = (-6.91 \pm 0.19) - (0.48 \pm 0.15) \times (z - 3) + (0.63 \pm 0.10)(M_B + 26) \quad (2)$$

in units of cubic megaparsecs. This equation is strictly valid for $M_B <= -25.6$, and employing it for intrinsically fainter objects requires that the luminosity function's slope does not change significantly, which we admit is an assumption. Nevertheless, using equation (2) to calculate the space density of objects at $z = 5$ with $-23 < M_B < -22$ gives a value of $\rho = 3 \times 10^{-6}$ Mpc^{-3}, which is similar to the mean OIRS space density. For the same range in M_B, we derive space densities of 3×10^{-5} and 1×10^{-5} Mpc^{-3} at redshifts of 3 and 4, respectively. At a redshift of 2, the 2dF cumulative luminosity function shown in equation (4) of Fan et al. (2001) gives $\rho = 1 \times 10^{-6}$ Mpc^{-3} for $M_{\rm B} < -25.5$. For a range in M_B from -25 to -24 the extrapolated space density would be $\sim 3 \times 10^{-6}$ Mpc^{-3}, which is also similar to the mean ρ for the OIRS population. Thus, within the uncertainties accrued by extrapolating the bright high-z quasar luminosity function to $M_B \sim -21$, we conclude that the averaged space density of OIRSs is consistent with that of lower luminosity AGN with redshifts $2 < z < 5$. Moreover, the distribution of q values for the OIRS population clearly implies a strong radio-loud AGN component.

The average space density of submillimeter galaxies provides another point of comparison. These objects are thought to be the progenitors of massive bulges that are powered primarily by heavily obscured star formation. Taking the sources detected at 850 μm by Barger et al. (1999) with fluxes greater than 2.2 mJy and assuming they lie between $1 < z < 3$ would result in a space density of $\rho_{850\,\mu{\rm m}} = 7 \times 10^{-5}$ Mpc^{-3}. This would be nearly 16 times larger than the average OIRS space density over the same redshift interval, which we determine to be $\rho_{\rm OIRS} = (4.1 \pm 0.8) \times 10^{-6}$ Mpc^{-3} if all OIRSs are within this interval. The submillimeter galaxies have a substantially larger space density. The discrepancy becomes even worse if one extrapolates the 850 μm source counts to fainter sources in order to account for the diffuse submillimeter background emission, in which case the average space density of submillimeter sources becomes comparable to the space density of present-day elliptical galaxies. Such a large difference in space density suggests that the OIRSs are not the objects that make up the submillimeter source population.

The average surface density of the 11 OIXSs is 157 ± 47 deg^{-2}. While formally $\sim$50% larger than that of the OIRS population determined in § 4.1, $\sigma_{\rm OIXS} \approx \sigma_{\rm OIRS}$ given the uncertainties. In § 4.3 we argued that 9 out of 11 are likely to have $1 < z < 5$ based on their X-ray hardness ratios. Distributing these uniformly over this redshift range gives an average space density $\rho_{\rm OIXS} = (3.9 \pm 1.3) \times 10^{-6}$ Mpc^{-3}, again comparable to $\rho_{\rm OIRS}$. Thus, the conclusions reached above for the OIRS population holds for OIXSs as well: $\rho_{\rm OIXS}$ is larger than the space density of local radio galaxies and luminous optically selected $1 < z < 5$ quasars but consistent with the space density of lower luminosity AGNs ($M_B > -23$) extrapolated from the quasar luminosity function of Fan et al. (2001). If four of the OIXSs are at $z \sim 4$–5, as is suggested by the HR values in Table 3 and Figure 6, then the OIXS space density over $1 < z < 3$ cannot be larger than $(3.3 \pm 1.5) \times 10^{-6}$ Mpc^{-3}, which is more than an order of magnitude smaller than the mean space density of Barger et al.'s (1999) $F_{850\,\mu{\rm m}} > 2.2$ mJy submillimeter sources. OIXSs do not appear to be the sources making up the submillimeter galaxy population.

While additional and independent observational evidence is clearly required to place these conclusions on a more solid footing, the estimated space densities of both OIRSs and OIXSs are consistent with lower luminosity AGN hosts ($M_B \gtrsim -23$) at $z \sim$ 1–5, suggesting that we are seeing the fainter end of the high-redshift quasar luminosity function.

5.2. *Do the Optically Invisible Radio and X-Ray Sources Represent Different Populations of AGNs?*

We concluded in § 4.2 that the OIRSs are predominately AGNs because of their 24 μm to 20 cm flux ratios, and we concluded in § 4.3 that the OIXSs are likewise primarily AGNs because of their low infrared to X-ray flux ratios. It is worth noting that these two independently derived samples of optically invisible AGNs do not overlap. In the common radio and X-ray survey region (Table 4) there are 10 OIRSs, none of which is detected in soft or hard X-ray bands by Wang et al. (2004). Similarly, there are 14 OIXSs within our VLA survey. None of these is detected at 20 cm.

We can ask whether this result is consistent with expectations from previous deep parallel surveys at radio and X-ray wavelengths. The most relevant study is that of Bauer et al. (2003) of the Chandra Deep Field North, which compared radio and X-ray sources at flux levels comparable to our sample. They used a variety of spectroscopic indicators, including optical and X-ray spectra to identify AGNs. Their results showed that such AGNs covered a wide range of X-ray to radio flux ratio. Specifically, they found (their Fig. 1) that AGNs could exist with $0.002 < F_{\rm X\text{-}ray}/F_{20\,\rm cm} < 2.5$, where $F_{\rm X\text{-}ray}$ is the *Chandra* full-band flux in units of 10^{-16} ergs s^{-1} cm^{-2}, and $F_{20\,\rm cm}$ is in units of microjanskys. The upper bound could even exceed 2.5, as this value derives from the upper limit of 40 μJy for the radio sources not detected in X-rays. From this, given that the faintest full-band X-ray flux in Wang et al.'s (2004) survey is 5×10^{-16} ergs s^{-1} cm^{-2}, an AGN could have a 20 cm flux density as high as $\sim$2 mJy and still not be detected in X-rays. Of our OIRS sample, only a source like 362 with $F_{20\,\rm cm} = 6.7$ mJy would have been easily detected in X-rays. The OIRSs' median 20 cm flux density is 400 μJy. For such a source to have a full-band X-ray flux less than 5×10^{-16} ergs s^{-1} cm^{-2} would imply $F_{\rm X\text{-}ray}/F_{20\,\rm cm} < 0.013$, which is well within the possible range found by Bauer et al. (2003).

Conversely, the median OIXS has full band X-ray flux of 5×10^{-15} ergs s^{-1} cm^{-2}. In order not to be detected in our radio survey, it would have to be fainter than 100 μJy, or have $F_{\rm X\text{-}ray}/F_{20\,\rm cm} > 0.5$, which is also well within the observed range of this ratio. We conclude, therefore, that the lack of overlap between the radio and X-ray samples of optically invisible AGN is consistent with the wide range of $F_{\rm X\text{-}ray}/F_{20\,\rm cm}$ that has been established among AGNs.

6. SUMMARY

We combined a *Spitzer* MIPS survey of the NDWFS Bootes field at 24 μm with an A-configuration VLA 20 cm survey of a 0.5 deg^2 subregion and a 172 ks *Chandra* observation to investigate the nature of optically "invisible" radio and X-ray

sources. These we define to be compact radio and X-ray sources without visible counterparts in the NDWFS B_W, R, and I images. It has been proposed that these objects represent populations of high-redshift galaxies harboring heavily obscured starbursts or AGNs. From the VLA and *Chandra* surveys we identify 31 OIRSs and 12 OIXSs within the area surveyed by MIPS at 24 μm, out of total radio and X-ray source populations of 377 and 168, respectively. Only 4 of the 31 OIRSs and none of the OIXSs are detected by MIPS at 24 μm. We compared the 20 cm and 24 μm emission properties of the OIRSs observed with MIPS with those expected from late spiral, ULIRG, Seyfert, and quasar SEDs over a wide redshift range. We conclude that the OIRSs are primarily a population of galaxies powered by AGNs, rather than dust-enshrouded starbursts, and that they likely lie at $z > 1$. Likewise, of the OIXSs with measured "soft" X-ray fluxes, all have 24 μm to 0.5–2 keV band flux ratio limits, consistent with a dominant and relatively unobscured AGN. The X-ray properties of OIXSs suggest that most are likely at $z > 1$, with several possibly at $z \sim 4$. Given the wide range in X-ray and radio properties of AGNs, the fact that the OIRSs and OIXSs have no object in common does not rule out their being from the same AGN source population.

Assuming the OIRSs populate the redshift range $1 < z < 5$, their average space density is $(2.4 \pm 0.5) \times 10^{-6}$ Mpc^{-3}. This is consistent with the space densities derived using the cumulative quasar luminosity function from Fan et al. (2001) over the redshift range $z = 2$–5 for $-23 < M_B < -22$, i.e., AGNs with blue luminosities comparable to current epoch Seyfert galaxies. The space density of 850 μm sources is much larger than this, suggesting that they are a fundamentally different class of object. Similarly, the OIXSs have an average space density of $(3.8 \pm 1.2) \times 10^{-6}$ Mpc^{-3} if they exist uniformly throughout the redshift range $1 < z < 5$, which is similar to that of the OIRSs. This is also consistent with the space density of lower luminosity AGNs extrapolated from Fan et al. (2001) for this redshift range.

We would like to thank Kevin Xu for access to his library of galaxy SEDs and both Robert Becker and David Helfand for valuable discussions. We also wish to thank the referee for suggestions that led to improvements in the manuscript. This work is based in part on observations made with the *Spitzer Space Telescope*, which is operated by the Jet Propulsion Laboratory, California Institute of Technology, under NASA contract 1407. Support for this work was provided by NASA through contract 1257184 issued by JPL at Caltech. The National Radio Astronomy Observatory is a facility of the National Science Foundation operated under cooperative agreement by Associated Universities, Inc. This publication made use of photographic data from the National Geographic Society-Palomar Observatory Sky Survey (NGS-POSS) obtained using the Oschin Telescope on Palomar Mountain. The NGS-POSS was funded by a grant from the National Geographic Society to Caltech. The plates were processed into the present compressed digital form with their permission. The Digitized Sky Survey was produced at the Space Telescope Science Institute under grant NAG W-2166. This research has also made use of the NASA/IPAC Extragalactic Database (NED), which is operated by JPL, Caltech, under contract with NASA.

REFERENCES

Appleton, P., et al. 2004, ApJS, 154, 147
Baars, J. W., Genzel, R., Pauliny-Toth, I., & Witzel, A. 1977, A&A, 61, 99
Barger, A. J., Cowie, L. L., & Sanders, D. B. 1999, ApJ, 518, L5
Barger, A. J., et al. 2003, AJ, 126, 632
Bauer, F., Alexander, D., Brandt, W., Hornschemeier, A., Vignali, C., Garmire, G., & Schneider, D. 2003, AJ, 126, 632
Becker, R., White, R., & Helfand, D. 1995, ApJ, 450, 559
Bell, E. F. 2003, ApJ, 586, 794
Bertin, E., & Arnouts, S. 1996, A&AS, 117, 393
Boyle, B. J., Shanks, T., Croom, S. M., Smith, R. J., Miller, L., Loaring, B., & Heymans, C. 2000, MNRAS, 317, 1014
Chary, R., & Elbaz, D. 2001, ApJ, 556, 562
de Jong, T., Klein, U., Wielbinski, R., & Wunderlich, E. 1985, A&A, 147, L6
de Vries, W. H., Morganti, R., Röttgering, H. J., Vermeulen, R., van Breugel, W., Rengelink, R., & Jarvis, M. J. 2002, AJ, 123, 1784
Fan, X., et al. 2001, AJ, 121, 54
Fomalont, E., Kellermann, K., Partridge, R., & Richards, E. 2002, AJ, 123, 2402
Haarsma, D. B., Partridge, R. B., Windhorst, R. A., & Richards, E. A. 2000, ApJ, 544, 641
Helou, G., Soifer, B. T., & Rowan-Robinson, M. 1985, ApJ, 298, L7
Higdon, S. J. U., et al. 2004, ApJS, 154, 174
Hopkins, A., Alfonso, J., Cram, L., & Mobasher, B. 1999, ApJ, 519, L59
Houck, J. R., et al. 2004, ApJS, 154, 18
Houck, J. R., et al. 2005, ApJL, 622, L105
Jannuzi, B., & Dey, A. 1999, in ASP Conf. Ser. 191, ed. R. Weymann et al. (San Francisco: ASP), 111
Marzke, R. O., Geller, M. J., Huchra, J. P., & Corwin, H. G., Jr. 1994, AJ, 108, 437
Lagache, G., Dole, H., & Puget, J. 2003, MNRAS, 338, 555
Osterbrock, D. E. 1989, Astrophysics of Gaseous Nebulae and Active Galactic Nuclei (Mill Valley: University Science Books)
Papovich, C., et al. 2004, ApJS, 154, 70
Rhoads, J., Malhorta, S., Dey, A., Stern, D., Spinrad, H., & Jannuzi, B. T. 2000, ApJ, 545, L85
Richards, E. A., Fomalont, E. B., Kellermann, K. I., Windhorst, R. A., Partridge, R. B., Cowie, L. L., & Barger, A. J. 1999, ApJ, 526, L73
Rieke, G. H., et al. 2004, ApJS, 154, 25
Schmidt, M., Schneider, D. P., & Gunn, J. E. 1995, AJ, 110, 68
Wang, J. X., Malhotra, S., Rhoads, J., Brown, M., Dey, A., Heckman, T., Jannuzi, B., Norman, C., Tiede, G., & Tozzi, P. 2004, AJ, 127, 213
Warren, S. J., Hewett, P., & Osmer, P. S. 1994, ApJ, 421, 412
Weedman, D., Charmandaris, V., & Zezas, A. 2004, ApJ, 600, 106
Werner, M. W., et al. 2004, ApJS, 154, 1
Xu, C., Lonsdale, C. J., Shupe, D. L., O'Linger, J., & Masci, F. 2001, ApJ, 562, 179
Yun, M., Reddy, N., & Condon, J. 2001, ApJ, 554, 803